SIAM J. SCI. COMPUT.
Vol. 30, No. 2, pp. 895–915

DYNAMIC PHASE BOUNDARIES FOR COMPRESSIBLE FLUIDS*

T. LU†, Z. L. XU‡, R. SAMULYAK†, J. GLIMM§, AND X. M. JI§

Abstract. We present an algorithm for the simulation of a generalized Riemann problem for phase transitions in compressible fluids. We model the transition as a tracked jump discontinuity. The emphasis here is on the coupling of the phase transition process to acoustic waves, which is required for the study of cavitation induced by strong rarefaction waves. The robustness of the proposed algorithm is verified by application to various physical regimes.

Key words. phase transition, conservative tracking

AMS subject classifications. 65M06, 65Z05

DOI. 10.1137/060661703

1. Introduction.

The coupling of hydrodynamics and thermal effects in liquid-vapor phase transitions is encountered in many applications such as evaporators and condensers for thermal control devices. Understanding of liquid-vapor phase changes therefore remains of great scientific and practical interest. In addition to transport phenomena within each individual phase in these processes, other phenomena may occur from the interface motion and thermal nonequilibrium effects. A complete macroscopic description of phase changes requires the coupling of hydrodynamics with surface tension, latent heat, interphase mass transfer, discontinuous material properties, nonequilibrium thermodynamics, etc. On the other hand, these phenomena occur on the phase boundary at different length scales and are coupled together. For example, the hydrodynamics at the macro scale is coupled to the thermal diffusion length scale, which starts at a nano scale. To simulate phase transitions accurately, phenomena at different scales must be understood and incorporated. Due to the multiscale characteristic and also due to the poor understanding of some of the physical mechanisms involved, the development of a numerical method for the modeling of phase transition is a challenge.

The earlier studies of the boiling process followed two major approaches. One examined the nature of the liquid-vapor phase change from a molecular point of view. For example, the rate of phase change was found to be proportional to the deviation from phase equilibrium according to a simplified model based on kinetic theory [1]. The relations between the molecular behavior and the macroscopic characteristics of vapor can be understood qualitatively at the molecular level. Part one of [5] gives an overview of this subject. By using molecular dynamics simulations, such phenomena as liquid films on a solid surface [29] and a liquid droplet in contact with a solid surface [19] have been studied. However, the molecular dynamics simulations are often not applicable to large complex applications due to limits of computational resources.

*Received by the editors June 1, 2006; accepted for publication (in revised form) June 25, 2007; published electronically February 22, 2008. This work was supported in part by National Science Foundation DMS-0102480 and Army Research Office grant W911NF0510413.

http://www.siam.org/journals/sisc/30-2/66170.html

†Computational Science Center, Brookhaven National Laboratory, Upton, NY 11973-6000 (tlu@nbl.gov, rosamu@bnl.gov).

‡Department of Mathematics, University of Notre Dame, Notre Dame, IN 46556 (zxu2@nd.edu).

§Department of Applied Mathematics and Statistics, University of Stony Brook, Stony Brook, NY 11794-3600 (glimm@ams.sunysb.edu, xji@ams.sunysb.edu).

The more practical approach for a large scale problem was based on simple models of vapor bubble dynamics. Rayleigh [26] formulated a simplified equation of motion for inertia-controlled growth of a spherical vapor bubble. Plesset and Zwick [22] and later Plesset and Prosperetti [23], among others, extended Rayleigh's analysis. Hao and Prosperetti [15] investigated the dynamics of bubbles in acoustic pressure fields assuming the vapor was saturated. These models, based on the Rayleigh–Plesset equation for incompressible liquid or the Keller equation of first order in c_l^{-1} for weakly compressible liquid, focused on the motion of a single spherical bubble under ambient pressure waves in liquid.

More recently, the second approach has been extended to simulations of vapor and liquid as separated phases with phase boundaries explicitly tracked. Welch [32] studied compressible two-phase flows including interface tracking with mass transfer while the phase interface was assumed to exist in thermal and chemical (Gibbs potential) equilibrium. Son and Dhir [30] employed a level set method to study film boiling near critical pressures. Juric and Tryggvason [17] simulated boiling flows in incompressible fluids using a nonequilibrium phase transition model with a parameter called kinetic mobility whose value was measured experimentally. Preston, Colonius, and Brennen [25] computed the growth and collapse of vapor bubbles traveling through a nozzle, in which the interfacial dynamics of phase transitions was derived from kinetic theory consideration. More discussion about this approach can be found in Preston's thesis [24] and references therein. Matsumoto and Takemura [20] studied numerically the influence of internal phenomena on the motion of a single spherical gas bubble with complete mass, momentum, and energy conservation laws for compressible fluids and the interfacial dynamics of phase transitions. Their governing equations contain more technical details, such as the concentration of noncondensable gas in the liquid and vapor phases. In [20], the temperature field was first solved from simplified energy equations, and other fluid fields were solved afterwards. In our approach, all fluid fields are updated simultaneously, and both thermodynamic and mechanical states at the interface are updated as coupled according to the proposed solution of the phase boundary Riemann-type problem. The dynamics of the phase boundary in our approach is explicitly coupled to acoustic waves in both phases. There are also some differences in assumptions simplifying the governing equations and in the numerical methods. In contrast to [20], we do not assume constant latent heat and achieve exact energy conservation by solving the generalized Hugoniot relation, derived in section 2.

The Riemann problem for compressible fluids undergoing phase transitions was studied by Menikoff and Plohr [21]. However, in their work, the phase transition zone was treated as a macroscopic mixture of two phases at equilibrium, as opposed to the sharp interface model studied in our work.

The description of the phase boundary evolution (generalized Riemann problem for the phase boundary), in which the phase boundary is treated as an explicitly tracked discontinuity in the present paper, resembles some features of both the classical Stefan problem [28] and the theory of deflagration waves in combustion [6]. The Stefan problem studies heat transfer-driven phase change (melting and solidification) for incompressible materials. Governed by parabolic equations, the Stefan problem neglects acoustic waves in liquids and solids and is usually solved by the phase field methods. For detailed discussions about the phase field methods, see [3, 4] and references therein. In contrast to the Stefan problem, the theory of deflagration waves in combustion solves equations for compressible media. The energy difference between

the phases (burnt and unburnt) in combustion, which is the heat released or absorbed in a chemical reaction, is analogous to the latent heat of vaporization in phase transitions. However, in a combustion problem, the energy difference between the phases is not associated with temperature gradients through the Hugoniot relation as in phase transitions. Temperature gradients are often neglected in practical calculations of combustion problems, while they cannot be neglected in phase transition problems studied in this paper.

In the present paper, equations for compressible fluids, containing heat diffusion terms, couple to the phase transition interface conditions. Using results for kinetic theory, conditions at the phase boundary account for deviations from the equilibrium given by the Clausius–Clapeyron equation. The governing system of equation is not hyperbolic, but it is still formally advection dominant. Since the solution of such a system loses the self-similarity property of Riemann solutions for hyperbolic systems, the phase boundary problem is not a Riemann problem in the strict sense; rather it is a problem with Riemann data, i.e., piecewise constant initial data with a jump in the middle. However, we still use the term "Riemann problem" in the present paper. As we are interested in an accurate algorithm for the evolution of the phase boundary, we solve a one-dimensional (1D) problem in the direction normal to the interface. The algorithms can be used without changes in multidimensional front tracking [9] for the normal interface propagation.

The paper is organized as follows. Section 2 describes the mathematical formulation of the phase transition problem. Section 3 discusses the numerical algorithms used to propagate the phase boundary and state values at grid cells near the phase boundary. In section 4 we present validation calculations and accuracy analysis.

2. Mathematical formulation. The physics of liquid-vapor phase transition is governed by the compressible Euler equations with heat diffusion. For the 1D algorithm, the equations are

$$\frac{\partial U}{\partial t} + \frac{\partial F(U)}{\partial x} = 0, \tag{2.1}$$

where $U = [\rho, \rho u, \rho E]$, $F(U) = [\rho u, \rho u^2 + P, (\rho E + P)u + q]$. ρ, P, u stand for density, pressure, and velocity, respectively. $E = u^2/2 + \epsilon$ is the specific total energy, with ϵ being the specific internal energy, which is associated with ρ and P through the equation of state for each phase. The thermal flux q follows Fourier's law of heat conduction:

$$q = -\kappa \frac{\partial T}{\partial x}, \tag{2.2}$$

where κ is thermal conductivity and T is temperature. The thermal diffusion changes the type of (2.1) from hyperbolic to parabolic. In the model presented here, the phase boundary is regarded as a sharp interface at which density is discontinuous. The normal velocity is also discontinuous across the interface due to mass conservation; i.e., the velocity field in the Knudsen layer is not resolved. Compared to the temperature field, which is required to be continuous across the phase boundary, the velocity field in each phase is much smoother (the gradient is small). As a result, viscosity plays a minor role compared to the thermal conduction in our algorithm and simulations and is omitted from (2.1).

In hyperbolic conservation laws, shock waves and contact discontinuities propagate as sharp discontinuities in the solution. The introduction of the heat diffusion

removes jump discontinuities in temperature waves but still allows discontinuities in pressure and velocity distributions. We can view (2.1) as modified Euler equations, which have modified solutions. In the present paper, the phase boundary is modeled as a tracked interface, in analogy with the contact discontinuity in classical Riemann solutions, but with nonzero mass flux. In the following derivation of jump conditions for a dynamic liquid-vapor phase boundary, subscripts v and l represent vapor and liquid, respectively, the square bracket stands for the jump across the phase boundary, and the bar stands for the average between two phases. For example, $[\rho] = \rho_{\rm v} - \rho_{\rm l}$, $\bar{u} = (u_{\rm l} + u_{\rm v})/2$. The velocity of the phase boundary is denoted by σ.

Integrating (2.1) across the interface, we obtain the balance equations for the mass, momentum, and total energy:

$$\sigma[\rho] = [\rho u], \tag{2.3}$$

$$\sigma[\rho u] = [\rho u^2 + p] + p_s, \tag{2.4}$$

$$\sigma[\rho E] = [u(\rho E + p) - \kappa T_{,x}] + \bar{u} p_s. \tag{2.5}$$

In (2.4), $p_s = \gamma(1/R_1 + 1/R_2)$ is the well-known pressure jump in the Laplace equation, with γ being the surface tension and R_1 and R_2 being radii of curvature. (2.3), (2.4), and (2.5) can be manipulated to yield equations for the mass flux, linear momentum flux, and energy balance at the phase boundary. For the mass flux $M = \rho_{\rm v}(u_{\rm v} - \sigma) = \rho_{\rm l}(u_{\rm l} - \sigma)$, the mass and momentum balance equations give

$$M = \frac{[u]}{[\tau]} = -\frac{[p] + p_s}{[u]}, \tag{2.6}$$

where $\tau = 1/\rho$. Combination of these equations with the energy balance equation leads to the generalized Hugoniot relation

$$\epsilon_{\rm v} - \epsilon_{\rm l} + \bar{p}(\tau_{\rm v} - \tau_{\rm l}) = \frac{1}{M}(\kappa_{\rm v} T_{{\rm v},x} - \kappa_{\rm l} T_{{\rm l},x}). \tag{2.7}$$

The left side is called the latent heat of the phase transition, which is often denoted by L. At phase equilibrium, L equals the difference between the specific enthalpy of two phases. We also postulate that the temperature is continuous across the phase boundary. Therefore, the interfacial temperatures of the vapor and liquid are equal:

$$T_{\rm l} = T_{\rm v} = T_{\rm s}, \tag{2.8}$$

where $T_{\rm s}$ is the interface temperature. This approach was also used in [16].

2.1. Interfacial mass flux. In the above discussion, neither the interface temperature $T_{\rm s}$ nor the mass flux M is determined. To close the equations we need another equation that determines either of them or relates them. We notice that the pressure is not continuous across the phase boundary as required by (2.6), unless $M = 0$. Physically, the pressure jump is a consequence of the velocity difference and the acceleration of the particles as they pass through the phase transition layer. The velocity difference in turn results from the large density difference between liquid and vapor and the conservation of mass. In dynamic phase transitions, deviation from thermal equilibrium at the interface drives the mass transfer across the interface.

Phase change is a complicated phenomenon of the interaction of vapor molecules with the liquid surface. Therefore, it is essential to examine phase transitions from a

kinetic theory point of view before we consider the macroscopic aspects of the phase change process. The derivation below follows Alty and Mackay [1]. Assuming the Maxwellian distribution of the velocity of vapor molecules, the number density is given as

$$n(\mathbf{u}) \propto \exp\left(-\frac{mu^2}{2k_BT}\right), \tag{2.9}$$

where m is the molecular mass and k_B the Boltzmann constant. The total mass flux of vapor molecules hitting the interface is

$$m\int\int\int_{u_x>0} du_x du_y du_z n(\mathbf{u}) u_x$$

$$= mN\bar{u}_x = \frac{mN}{4}\bar{u} = \frac{p_{\mathrm{v}}}{\sqrt{2\pi RT}},$$

where N is the total number of molecules per unit volume and $R = k_B/m$. Not all molecules hitting the phase boundary condense into liquid. The ratio of molecules condensing into liquid over the total number hitting the phase boundary is called the *accommodation coefficient*. It is also referred to as the condensation or evaporation coefficient sometimes. We use the term accommodation coefficient and denote it by α. The range of α is between 0 and 1. The mass flux of the condensing vapor is

$$\alpha\frac{p_{\mathrm{v}}}{\sqrt{2\pi RT}}. \tag{2.10}$$

In the present analysis, we assume that the fluxes of condensing and vaporizing molecules can be derived separately and the results superimposed to obtain the net flux. Since the net mass flux cancels at equilibrium, the mass flux of evaporating liquid is the same as that of condensing vapor. Denoting the equilibrium pressure at temperature T by $p_{\mathrm{sat}}(T)$, the mass flux of the evaporating liquid is

$$\alpha\frac{p_{\mathrm{sat}}(T)}{\sqrt{2\pi RT}}. \tag{2.11}$$

Taking into account that the evaporation of liquid is mainly determined by the temperature, we find that the net mass flux of evaporation when the vapor is unsaturated or oversaturated is

$$M_{ev} = \alpha\frac{p_{\mathrm{sat}}(T) - p_{\mathrm{v}}}{\sqrt{2\pi RT}}. \tag{2.12}$$

The relations derived above clearly depend on the value of the accommodation coefficient. Research has indicated that the value of α less than 1 results from either impurity of substances or deficiency of the kinetic theory-based derivation. For example, the above analysis does not consider nonequilibrium interactions between molecules leaving the interface and those approaching the interface. For the detailed discussion of the accommodation coefficient, see [5] and references therein. A review of experiments and theories regarding the accommodation coefficient can also be found in [14]. In the present paper, different values of α are studied numerically.

In general, the interface temperature T_{s} is a nonlinear function of the mass flux M_{ev} and other state variables. It is difficult to obtain a closed form for T_{s}. The expression for the interface temperature is described in the following section.

3. Numerical methods. The numerical technique combines the conservative front tracking method [13] developed for multiphase flows with an algorithm designed for phase transitions. The tracked phase boundary is represented by an interface (or front) which in one dimension is a point advancing in a uniform underlying Eulerian grid. In higher dimensions, the phase boundary is an explicitly tracked codimension-1 manifold advancing Lagrangianly. The time stepping to advance solution states can be broken up into two main steps: the propagation of the front and the finite differencing for updating cell state values. See [2, 8, 9, 10] for details of the front-tracking method. The finite difference algorithm used in the present study is conservative for all grid cells, including the irregular ones cut by the front. It is a finite volume scheme, which updates the cell state average values. In this paper, we use the monotone upstream-centered schemes for conservation laws (MUSCL) type [18, 7] scheme for the reconstruction of piecewise linear states. The reconstructed state values are used to compute the numerical flux values across the volume boundaries and then update the cell states. The phase boundary propagation algorithm will be presented first, followed by an introduction to the conservative tracking finite differencing algorithm.

3.1. An iterative phase boundary solution algorithm. The phase boundary propagation algorithm determines solutions of a general phase boundary Riemann problem. The solution procedure is similar to that for a contact discontinuity. The key iterative step in the solution of a Riemann problem for a contact discontinuity is to find the mid state, based on equations of continuity of the velocity and pressure at the contact. We call this step the FMS (find mid state) iteration and generalize it to the case of discontinuous velocities and pressures across the phase boundary. The contact discontinuity propagation algorithm consists of three steps: the slope reconstruction step to compute approximations to the flow gradients, the prediction step using Riemann problem solutions to predict the new position of the point, and the correction step to account for flow gradients on either side of the front. For the phase boundary propagation algorithm, there is no prediction step because the exact solution structure is not known. The correction step moves the location of the phase boundary point and updates the phase boundary states.

The complete solution to the phase boundary Riemann problem is obtained by solving phase boundary conditions and generalized FMS equations consistently. Consistency means that the velocity jump and the pressure jump in the FMS must equal those given by the phase boundary conditions. The numerical algorithm for a dynamical phase transition proceeds as follows. The characteristic form of (2.1), which are the FMS equations used at the interface, is

$$\frac{\mathrm{d}p}{\mathrm{d}\lambda_+} + \rho c \frac{\mathrm{d}u}{\mathrm{d}\lambda_+} = \Gamma \kappa T_{xx}, \tag{3.1}$$

$$\frac{\mathrm{d}p}{\mathrm{d}\lambda_-} - \rho c \frac{\mathrm{d}u}{\mathrm{d}\lambda_-} = \Gamma \kappa T_{xx}, \tag{3.2}$$

$$\frac{\mathrm{d}\epsilon}{\mathrm{d}\lambda_0} + p \frac{\mathrm{d}\tau}{\mathrm{d}\lambda_0} = \frac{1}{\rho} T_{xx}, \tag{3.3}$$

where $c = \sqrt{(\frac{\partial p}{\partial \rho})_S}$ is the sound speed (S is the specific entropy) and Γ is the Gruneisen coefficient [21]. The characteristic derivatives λ_+, λ_-, and λ_0 are defined

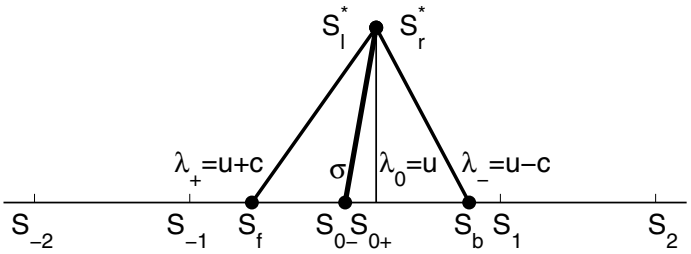

FIG. 1. *Stencil for the phase boundary propagation. The new front states S_l^* and S_r^* are calculated. The characteristic equations along $\lambda_\pm$ characteristics are used in the calculation, while the equation along the λ_0 characteristic is substituted for by thermal conditions at the phase boundary.*

by

$$\frac{\mathrm{d}}{\mathrm{d}\lambda_+} = \frac{\partial}{\partial t} + (u+c)\frac{\partial}{\partial x}, \tag{3.4}$$

$$\frac{\mathrm{d}}{\mathrm{d}\lambda_-} = \frac{\partial}{\partial t} + (u-c)\frac{\partial}{\partial x}, \tag{3.5}$$

$$\frac{\mathrm{d}}{\mathrm{d}\lambda_0} = \frac{\partial}{\partial t} + u\frac{\partial}{\partial x}. \tag{3.6}$$

The phase boundary conditions are (2.6)–(2.8) and (2.12).

To solve the characteristic system with the phase boundary conditions, an iteration algorithm which intertwines a hydro iteration and a thermal iteration is developed. In the hydro iteration, the characteristic system and the phase boundary conditions are used to solve for interfacial pressures and velocities. In the thermal iteration, the interface temperature and mass flux of evaporation are found. The iteration algorithm loops over these two subiteration steps until the solution converges. Backward characteristics are traced from an estimated location of the phase boundary at the next time step. States at the feet of these characteristics (at the current time level) are first obtained by interpolation. The characteristic speeds are $\lambda_\pm = u \pm c$ and $\lambda_0 = u$, while the phase transition interface moves at a speed $\sigma = [\rho u]/[\rho]$. For a small time step Δt, the characteristics are approximated by straight lines. Figure 1 is a schematic diagram showing the backward characteristics. The left foot is a distance $(c_l + u_l - \sigma)\Delta t$ away from the interface, while the right foot is a distance $(c_r - u_r + \sigma)\Delta t$ away from the interface. Since $|u-\sigma| \ll c$ in phase transitions, the feet of $\lambda_\pm$ characteristics always reside in the left and right sides of the phase boundary as shown in Figure 1. Once the states at the $\lambda_\pm$ characteristic feet are obtained by interpolation, (3.1) and (3.2) are integrated along the characteristics and then solved together with phase boundary conditions.

For phase transitions, the foot of λ_0 characteristic of each phase, located at $(\sigma - u)\Delta t$ relative to the interface, differs from the interface position. The side of the feet of λ_0 characteristics to the interface depends on the direction of the phase transition. Unlike the classical Riemann problem, where the two λ_0 characteristics meet at the interface and the state in each phase evolves adiabatically along the characteristic, the phase boundary propagation must be treated differently because of the heat diffusion and the mass transfer across the interface. Since the temperature equation is parabolic rather than hyperbolic, it must be solved numerically by using thermal conditions at the phase boundary, namely, (2.7), (2.8), and (2.12), rather than by integrating (3.3)

along the λ_0 characteristics. In the following paragraphs we describe the iteration algorithm in details:

1. *Thermal iteration.* Substitute the vapor pressure at S_{0+} for p_v in (2.12) and discretize (2.7). We have two equations which we solve for the two unknown variables T_s and M. The function p_{sat} is a nonlinear function. Since the thermal iteration is coupled to the hydro iteration where p_v is updated, the Clausius–Clapeyron equation is linearized at a reference temperature T_v and solved for T_s and M while preserving the convergence of S_l^* and S_r^* in Figure 1 through the iteration. For the first iteration step, T_v can be chosen to be equal to T_s at the beginning of the time step if $T_{0-} = T_{0+}$. For subsequent iteration steps, T_v is simply the T_s obtained in the previous iteration. Upon linearization, we obtain solutions

$$T_s = \frac{\kappa_l T_{-1} + \kappa_v T_1 + \frac{\alpha}{\sqrt{2\pi R T_v}} L\Delta x (p_v - p_{sat}(T_v) + \frac{\mathrm{d}p_{sat}}{\mathrm{d}T}(T_v)T_v)}{\kappa_l + \kappa_v + \frac{\alpha}{\sqrt{2\pi R T_v}} L\Delta x \frac{\mathrm{d}p_{sat}}{\mathrm{d}T}(T_v)} \tag{3.7}$$

and

$$M_{ev} = \frac{\alpha}{\sqrt{2\pi R T_v}} \left(p_{sat}(T_v) - p_v + \frac{\mathrm{d}p_{sat}}{\mathrm{d}T}(T_v)(T_s - T_v) \right), \tag{3.8}$$

where Δx is the grid size and $\frac{\mathrm{d}p_{sat}}{\mathrm{d}T}(T_v)$ is the slope of phase coexistence curve at T_v determined by the Clausius–Clapeyron equation. The latent heat L in (3.7) is approximately the equilibrium latent heat at temperature T_s.

2. *Hydro iteration.* Having obtained the temperature T_s and mass flux M_{ev}, we can solve the characteristic equations (3.1) and (3.2) combined with the Rankine–Hugoniot conditions (2.6). Integrated along the characteristics, (3.1) and (3.2) become

$$\int_{t_n}^{t_{n+1}} \frac{\mathrm{d}p}{\rho c} + \int_{t_n}^{t_{n+1}} \mathrm{d}u = \int_{t_n}^{t_{n+1}} \frac{\Gamma \kappa T_{xx}}{\rho c} \mathrm{d}\lambda_+, \tag{3.9}$$

$$\int_{t_n}^{t_{n+1}} \frac{\mathrm{d}p}{\rho c} - \int_{t_n}^{t_{n+1}} \mathrm{d}u = \int_{t_n}^{t_{n+1}} \frac{\Gamma \kappa T_{xx}}{\rho c} \mathrm{d}\lambda_-, \tag{3.10}$$

in the left and the right side of the interface, respectively. After forward Euler discretization, they become

$$\frac{p_l^* - p_f}{\rho_f c_f} + (u_l^* - u_f) = \frac{\Gamma_l \kappa_l}{\rho_f c_f} T_{l,xx} \Delta t, \tag{3.11}$$

$$\frac{p_r^* - p_b}{\rho_b c_b} - (u_r^* - u_b) = \frac{\Gamma_r \kappa_r}{\rho_b c_b} T_{r,xx} \Delta t, \tag{3.12}$$

where the symbols are in accordance with Figure 1 and T_{xx}'s are obtained by finite difference. (3.11) and (3.12) are then solved together with (2.6), which involves a term $[\tau]$. For the first iteration $[\tau]$ is set to the value at the beginning of the time step. For subsequent iteration steps, the density ρ_l^* and ρ_r^* are determined from their equations of state with the pressure and temperature obtained in the iteration and from which $[\tau]$ is updated.

3. *Convergence check.* Convergence of the iteration is controlled by p_v and $[\tau]$. The last step in each iteration is to compare the newly obtained p_v and $[\tau]$ with the values from the previous iteration. If the relative errors of both p_v and $[\tau]$ are smaller than given tolerances, the iteration is terminated; otherwise, p_v and $[\tau]$ are updated for the next iteration, which starts from step 1 again. In the present study, the tolerances of the relative errors for p_v and $[\tau]$ both have the value 10^{-9}.

The thermal iteration in the proposed algorithm depends on a subgrid model to describe the thermal layer at the phase boundary. The width of the thermal layer in each phase is proportional to $\sqrt{\nu t}$, where $\nu = \kappa/(\rho c_p)$ is the thermal diffusivity in each phase. The time step in simulations is restricted to $\Delta t < \Delta x/c$ by the Courant, Friedrichs, and Lewy (CFL) condition, which states that the domain of dependence of hyperbolic PDEs must lie within the domain of dependence of the finite difference scheme at each mesh point to guarantee the stability of an explicit finite difference scheme. It usually requires 10^3–10^4 steps for the liquid thermal layer to expand to a micron scale grid cell. If the thermal layer is thinner than a grid cell, the temperature gradient varying significantly within the cell makes conventional finite difference schemes insufficient in estimating the temperature gradient at the phase boundary, which is crucial for the calculation of the evaporation rate. When the thermal layer is thinner than a grid cell, the temperature profile in it takes the form

$$T \approx T_s + (T_1 - T_s)\mathrm{erf}\left(\frac{x}{\sqrt{4\nu t}}\right), \tag{3.13}$$

where T_s is the phase boundary temperature and T_1 is the temperature one grid cell away from the phase boundary. Thus the temperature gradient at the interface is approximated by

$$\frac{\partial T}{\partial x} \approx \frac{T_1 - T_s}{\sqrt{\pi \nu t}}. \tag{3.14}$$

In the iteration algorithm, the interfacial temperature gradient in the form of $\Delta T/\Delta x$ should be replaced by the above approximation. When the thermal layer is wider than a grid cell, the conventional finite difference approximation of the temperature gradient at the interface gives satisfactory results.

This is a new description of the generalized Riemann problem associated with a phase transition in a fully compressible fluid. Mass transfer across an interface due to the phase change is taken into account. The interface motion depends on the phase change under nonequilibrium thermodynamic and hydrodynamic conditions.

The following is the accuracy analysis of the iterative algorithm. To obtain the approximation of states at the feet of $\lambda_\pm$ characteristics, we use a second order MUSCL reconstruction. A piecewise linear function is reconstructed on each cell from cell-averaged values at time t^n to yield the approximate states $\mathcal{U}_f^n$ and $\mathcal{U}_b^n$ at the feet of characteristics such that the errors $\mathcal{U}_f^n - U_f^n = \mathcal{O}(\Delta x^2)$ and $\mathcal{U}_b^n - U_b^n = \mathcal{O}(\Delta x^2)$. By solving the generalized Riemann problem by the above algorithm with $\mathcal{U}_f^n$ and $\mathcal{U}_b^n$ as the initial states, we obtain a numerical phase boundary speed σ^{n+1} with error $\mathcal{O}(\Delta x)$ and approximate states on both sides of the phase boundary also with accuracy of first order in Δx. The reason is that (3.9) and (3.10) are solved by forward Euler discretization, which is of first order accuracy. One of the reasons for not using a higher order algorithm at the interface is that the second order MUSCL scheme used in the interior of both phases reduces to first order in the presence of shock waves.

3.2. Conservative finite differencing. In the implementation of the conservative tracking algorithm, the phase boundary is tracked as an interface in space and time. The linear approximation of the space-time interface is formed by connecting spatial interfaces at two consecutive time steps. We connect the nodes of a spatial cell at time t_n to the nodes of the corresponding cell at time t_{n+1} to form a space-time volume. If a space-time interface passes through the interior of a space-time volume, the volume is divided into fragments such that the space-time interface is on the boundary of the fragments. These volume fragments are combined with corresponding neighbors to alleviate the restriction by the CFL condition. A second order Godunov-type finite volume differencing scheme is used to update the grid states. On space-time interfaces, the dynamic flux, which is $F - \sigma U$ resulting from the Rankine–Hugoniot conditions of (2.1), replaces the usual flux F for time-independent boundaries of the space-time volumes. This redefinition gives equal values of fluxes when evaluated from both sides of the space-time interface, so that the conservation laws are satisfied exactly at the tracked interface. Details of the conservative finite differencing method can be found in [13].

For the proposed algorithm, as pointed out in section 3.1, the velocity of the phase boundary and the interface states calculated numerically are of first order accuracy in Δx because the characteristic equations (3.9) and (3.10) are solved by forward Euler discretization. Therefore, the position of the phase boundary, denoted by $S(t)$, is also of first order accuracy because

$$\begin{aligned}\mathcal{S}(t) &= \mathcal{S}(0) + \int_0^t \sigma_{num}(\tau)d\tau \\ &= S(0) + \int_0^t [\sigma_{exact}(\tau) + \mathcal{O}(\Delta x)]d\tau \\ &= S(t) + \mathcal{O}(\Delta x). \end{aligned} \tag{3.15}$$

Furthermore, the discretization of the flux across the interface

$$F_s^{n+1/2} = \frac{1}{\Delta t}\int_{t_n}^{t_{n+1}} [F(U_s(t)) - \sigma U_s(t)]dt \tag{3.16}$$

by

$$\mathcal{F}_s^{n+1/2} = \frac{1}{2}[F(\mathcal{U}_s^n) - \sigma^n \mathcal{U}_s^n + F(\mathcal{U}_s^{n+1}) - \sigma^{n+1}\mathcal{U}_s^{n+1}] \tag{3.17}$$

using the trapezoidal rule is also of first order accuracy in Δx, in contrast to [13], where the conservative finite differencing is uniformly second order accurate in L_1. Nevertheless, the proposed algorithm is one order more accurate than any capturing algorithm, because at solution of discontinuities, the local truncation errors of the capturing algorithms are typically $\mathcal{O}(1)$ [27, 12, 11].

4. Simulation results. In this section, simulation results for various test problems are presented and analyzed. In sections 4.1 and 4.2, shock waves and rarefaction waves interacting with a phase boundary are simulated, and results are used to test the accuracy and convergence of the proposed algorithm. The influence of the accommodation coefficient is studied in section 4.3. Phase transitions controlled by external heat flux are simulated in section 4.4. Finally, a test problem in section 4.5 demonstrates two-phase flow in the presence of both acoustic and thermal waves. Only the

phase boundary was tracked for all computations; shock fronts were captured by the MUSCL scheme. The order of accuracy was determined by the following expression:

$$\text{order} = \log_2 \frac{\text{L}_1 \text{ error in grid}(2 \triangle x)}{\text{L}_1 \text{ error in grid}(\triangle x)}. \tag{4.1}$$

We should note here that the L_1 error includes both the solution state error and the interface position error since we have tracked phase boundaries in solutions. The material used for simulations in sections 4.1–4.3 is n-heptane. The equation of state (EOS) for n-heptane vapor used in the simulations was a γ-law gas, with $\gamma = 1.05$. The thermal conductivity of the vapor was estimated to be $\kappa = 0.013$ W/mK. The EOS for liquid n-heptane was given by a stiffened polytropic equation [21]

$$P + \gamma P_\infty = (\gamma - 1)\rho(E + E_\infty), \tag{4.2}$$

with adiabatic exponent $\gamma = 3.19$, stiffening constant $P_\infty = 3000$ bar, and energy translation $E_\infty = 4.85 \times 10^9$ erg/g. The thermal conductivity of the liquid n-heptane was set to $\kappa = 0.13$ W/mK. The thermodynamic properties of n-heptane are described in [31]. In sections 4.4 and 4.5, the material used in simulations was water and its vapor. Parameters for their equations of state were set correspondingly.

4.1. A phase boundary-shock tube problem. We consider the interaction of a shock wave with a phase boundary. The computational domain is [0.2–0.8] cm, with the vapor-liquid interface located at 0.65 cm initially. The forward shock wave is located at 0.5 cm in the liquid initially. The preshock states are at phase equilibrium, and the initial conditions are

$$U(0.5 < x \le 0.65, t = 0) = \begin{pmatrix} \rho \\ u \\ p \end{pmatrix} = \begin{pmatrix} 0.633 \\ 0 \\ 0.112 \end{pmatrix},$$

$$U(0.65 < x \le 0.8, t = 0) = \begin{pmatrix} \rho \\ u \\ p \end{pmatrix} = \begin{pmatrix} 0.00043 \\ 0 \\ 0.112 \end{pmatrix}. \tag{4.3}$$

The pressure behind the shock front is $p = 8$ bar. A flowthrough boundary condition is used on both the left and the right boundaries. We used four meshes with 450, 900, 1800, and 3600 cells, respectively.

The results for 3600 cells at time 2 μs are shown in Figure 2. The phase boundary moves to the right by 1.58 μm at this time. The spike in the temperature plot shows the vapor heated by the shock wave. If the phase boundary were treated as a contact discontinuity, after the interaction of the contact and the shock wave, the solution of this Riemann problem would consist of a backward rarefaction wave, a contact discontinuity, and a forward shock wave. The solution of the contact-shock wave interaction and the solution of the phase boundary-shock wave interaction are visually identical in this case. It indicates that thermal waves or phase nonequilibrium must be present for phase transitions to play an important role. If the vapor and liquid are at phase equilibrium initially and there is no external heat flux as in this problem, the phase transition induced by shock waves is very weak. In fact, the position difference between the phase boundary and the contact interface is less than 0.1% at as late as 3 ms. However, the advection-dominated problem serves well for the study of convergence of the algorithm because shock fronts are usually where numerical schemes have the least accuracy. The accuracy results of this set of simulations are shown in Table 1. It is clear that the algorithm has more than first order accuracy.

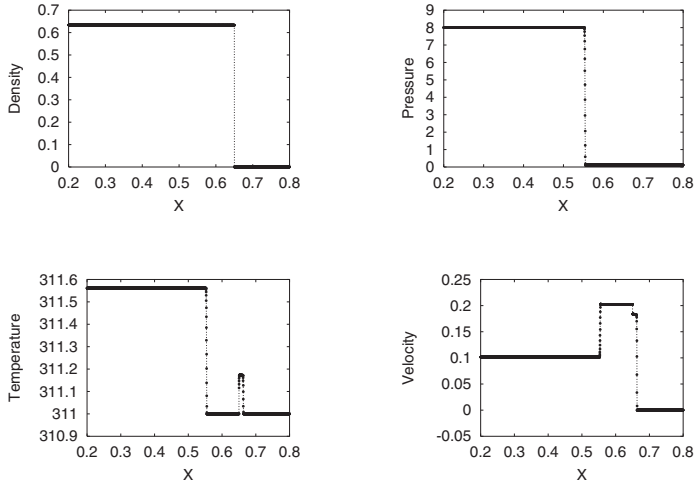

FIG. 2. *Solution of phase boundary-shock wave interaction problem: density, pressure, temperature, and velocity at 2 μs. X is in cm, and the units of the variables are g/cm^3, bar, Kelvin, and cm/ms, respectively.*

TABLE 1
Accuracy and convergence rate for phase boundary-shock wave interaction.

	Mass		*Momentum*		*Energy*	
N	L_1 error	Order	L_1 error	Order	L_1 error	Order
450	1.849E-6	-	1.128E-4	-	4.366E-3	-
900	6.182E-7	1.580	5.054E-5	1.158	1.258E-3	1.795
1800	2.189E-7	1.498	1.832E-5	1.464	4.407E-4	1.513

4.2. A phase boundary-rarefaction wave problem. In this section, we describe a phase boundary-rarefaction wave interaction problem. The computational domain is still [0.2–0.8] cm. Initially, the vapor-liquid interface is located at 0.54 cm, and the forward rarefaction wave of width 0.001 cm is located at 0.5 cm in liquid. The initial states of both phases ahead of the rarefaction wave are the same as in the phase boundary-shock wave problem in section 4.1. The pressure at the trailing edge of the rarefaction wave is $p = -20$ bar. A flowthrough boundary condition is used on both ends of the computational domain.

The results for 3600 cells at time 1 μs are shown in Figure 3. The phase boundary has moved to the left by 3.54 μm by then. As in section 4.1, the solution would be virtually unchanged if the phase boundary were treated as a contact discontinuity. After the interaction of the contact and the rarefaction wave, the solution of this Riemann problem consists of a backward shock wave, a contact discontinuity, and a forward rarefaction wave. Again, due to the lack of external heat flux or deviation from phase equilibrium, phase transitions are minimal. At 3 ms, the position difference between the phase boundary and the contact interface is less than 0.5%. The accuracy results of this set of simulations are shown in Table 2. It confirms that the algorithm has consistently more than first order accuracy.

4.3. Influence of α on the solution. We investigated the influence of the accommodation coefficient α on the phase boundary evolution. We tested the above

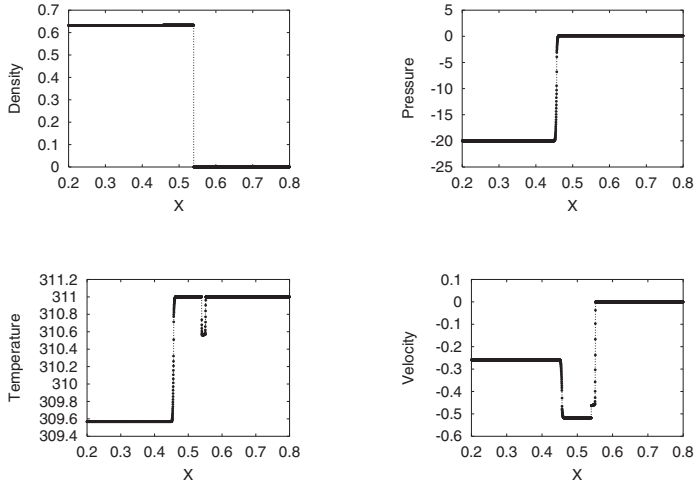

FIG. 3. *Solution of phase boundary-rarefaction wave interaction problem: density, pressure, temperature, and velocity at* 1 μs. *X is in cm, and the units of the variables are* g/cm^3, *bar, Kelvin, and* cm/ms, *respectively.*

TABLE 2
Accuracy and convergence rate for phase boundary-rarefaction wave interaction.

	Mass		*Momentum*		*Energy*	
N	L_1 error	Order	L_1 error	Order	L_1 error	Order
450	4.058E-6	-	2.362E-4	-	8.314E-3	-
900	1.417E-6	1.518	1.218E-4	0.955	2.925E-3	1.507
1800	5.103E-7	1.474	4.012E-5	1.602	1.040E-3	1.492

phase boundary-rarefaction wave problem with $\alpha = 0.2$, 0.4, 0.6, and 0.8, respectively. The computation domain was extended to [0.1–0.8] cm to accommodate the simulation time. Figure 4 shows a magnified view of the velocity plot at 1 μs for a simulation with 3600 cells.

We expect that, under the same condition, the larger the α value, the faster the evaporation process. This is confirmed by the present numerical experiment. From Figure 4, we can see that a larger α value is associated with a larger velocity jump across the phase boundary, which corresponds to a larger evaporation rate. The positions of the phase boundary at various times corresponding to the above α values are listed in Table 3. From the table, we see that the phase boundary moves to the left faster for a larger accommodation coefficient. This confirms that a larger α gives a higher evaporation rate, which enhances the expansion of vapor due to the rarefaction wave more strongly. Nevertheless, the influence of the α on the phase boundary dynamics is insignificant in this case since the case is in the advection-dominated regime.

4.4. A thermal wave problem. From the previous examples we see that phase transitions play a minor role in advection-dominated problems, such as the passage of a shock or rarefaction wave of moderate strength through an equilibrium phase boundary. However, the mass transfer in phase transitions does play an important role in the presence of a sustained thermal wave. Here we used the numerical method

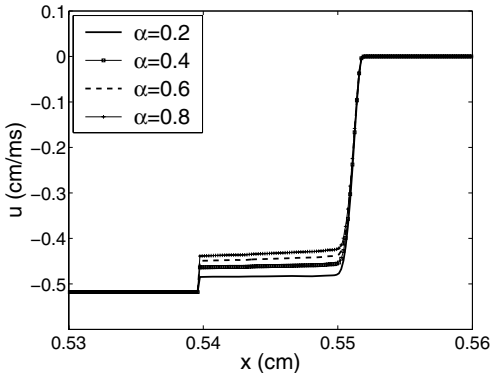

FIG. 4. *The enlarged velocity plot of the phase boundary region at* 1 μs *for the phase boundary-rarefaction wave interaction problem. The curves are obtained using different accommodation coefficients* α.

TABLE 3
Phase boundary positions.

α	$t = 0.001$ ms	$t = 0.05$ ms	$t = 0.1$ ms
0.2	0.53734604	0.34516851	0.14909711
0.4	0.53734596	0.34516649	0.14909417
0.6	0.53734590	0.34516538	0.14909265
0.8	0.53734586	0.34516467	0.14909170

to simulate the condensation of water vapor under outgoing heat flux. The early-stage buildup of the temperature field has been demonstrated. The late-stage condensing flow was compared to the exact steady states and the convergence was confirmed.

The test problem consists of a tube containing a shallow layer of water. The bottom of the tube is in contact with colder material to sustain a constant outgoing heat flux. The remaining space is filled with water vapor. Initially the water and water vapor are at rest and in equilibrium at room temperature: $T_0 = 20^\circ$C, $p_0 = 23.4$ mbar. The outgoing heat flux from water gradually builds up a temperature gradient in the water and causes condensation. For the boundary conditions at the opening of the tube, the vapor pressure is assumed to be constant, and the temperature gradient is assumed to be zero:

$$\left(\frac{\partial T}{\partial x}\right)_{x=0} = 0, \quad p(x=0) = p_0;$$

$$\left(\frac{\partial T}{\partial x}\right)_{x=D} = T_{x0}, \quad u(x=D) = 0.$$

Here $D = 0.1$ mm is the total length of the liquid and vapor in the calculation. $x = D$ is the bottom of the tube, and $x = 0$ is the vapor end. In the following example, $T_{x0} = -2.5^\circ\text{C}/\mu\text{m}$. The EOS parameters for water and water vapor are set by their physical properties at room temperature. Their thermal conductivities are 0.598 and 0.0182 W/mK, respectively. The latent heat of evaporation is 2450 J/g, and the evaporation coefficient is set to 0.4.

4.4.1. Early stage. The grid size of the simulation was 1 μm. The position of the phase boundary x_{ph} calculated from the simulation is plotted against the time

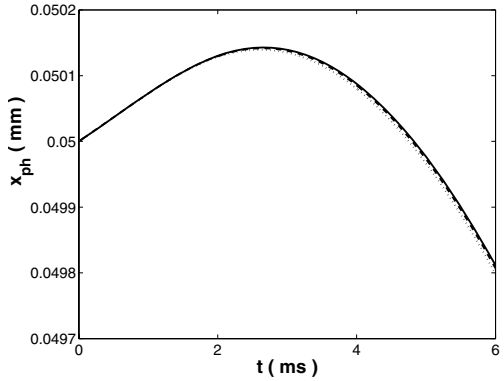

FIG. 5. *The position of phase boundary in the first* 6 *ms.* $T_0 = 20°\text{C}$, $p_0 = 23.4$ *mbar,* $T_{x0} = -2.5°\text{C}/\mu\text{m}$. x_{ph} *first increases due to the thermal contraction and later decreases due to condensation. The solid line is from the simulation with grid size* 1 μm*, the dashed line is with grid size* 2 μm*, and the dotted line is with grid size* 4 μm.

$0 < t < 6$ ms in Figure 5. It shows that the phase boundary first moves to the water end and then back to the vapor end. In other words, before the liquid volume increases due to the condensation, it first decreases for about 2.7 ms. The reason is that the liquid shrinks with the lowering temperature when the heat flux required for the phase transition has not been built up. It is not until about $t = 4.8$ ms that the phase boundary moves back to the original position. After that the phase transition dominates over thermal contraction of the liquid, and the phase boundary moves steadily toward the vapor end.

4.4.2. Late stage. The liquid volume increases during the condensation, while the thermal and pressure waves in the tube gradually approach the "steady state" dictated by the boundary conditions and liquid height. The steady state is not a single state but rather a family of states depending on the liquid height, which varies with time. The steady state is uniform in vapor by the boundary condition. In the liquid phase, since the Mach number $\ll 1$, the energy conservation law in (2.1) can be approximated by a temperature equation as in Stefan's problem,

$$\rho c_p \left(\frac{\partial T}{\partial t} + u \frac{\partial T}{\partial x} \right) = \kappa \frac{\partial^2 T}{\partial x^2},$$

where c_p is the specific heat at constant pressure, and the energy equation at the phase boundary (2.7) becomes

$$(\kappa T_x)_s = -ML,$$

where L is the latent heat of the phase transition and M is the transition rate. The temperature field evolves into the following steady state:

$$T(x) = T_s + \frac{L}{c_p} \left(1 - \exp\left(\frac{M c_p (x - x_{ph})}{\kappa} \right) \right), \tag{4.4}$$

where x_{ph} is the location of the phase boundary and T_s is the interface temperature. For each x_{ph}, M is determined by the specified temperature gradient at the water end. T_s can be found from M via the kinetic relation with known vapor pressure p_0. The steady state liquid pressure p_l, the velocity of the phase boundary u_{ph}, and the

TABLE 4

Comparison of the actual states from simulation with the corresponding steady states at various times. The steady state depends on the interface position at time t.

$t(ms)$	10		20		30	
$x_{ph}(mm)$	0.04874		0.04464		0.03991	
state	actual	steady	actual	steady	actual	steady
$M(10^{-5}g/cm^2 \cdot ms)$	3.61	5.10	4.74	5.04	4.958	4.968
$T_s(^oC)$	14.09	11.65	12.24	11.75	11.880	11.865
p_l(mbar)	23.48	23.56	23.535	23.552	23.5475	23.5481
$u_{ph}(10^{-5}cm/ms)$	-3.31	-4.97	-4.58	-4.90	-4.818	-4.822
$u_v(cm/ms)$	2.16	3.06	2.84	3.02	2.975	2.981

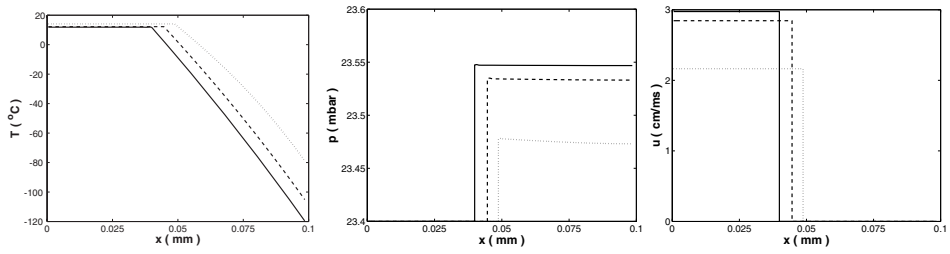

(a) (b) (c)

FIG. 6. *Late-stage condensing flow.* $T_0 = 20°\text{C}$, $p_0 = 23.4$ *mbar,* $T_{x0} = -2.5°\text{C}/\mu\text{m}$. *Dotted curves are for* $t = 10$ *ms, dashed curves are for* $t = 20$ *ms, and solid curves are for* $t = 30$ *ms.*

vapor velocity u_v can all be calculated using the steady state form of solutions to the mass and momentum conservation laws in (2.1). Since the phase boundary is moving, all of the quantities above vary with time.

Table 4 is the comparison between the steady state quantities and the corresponding ones in the evolving wave obtained from numerical simulation. It can be seen from the table that the evolving state is closer to the steady state at later time. Figure 6 visualizes the evolution. From the figure we see that the pressure and velocity jumps at the phase boundary increase steadily toward the values of steady states.

We compared the liquid temperature field in Figure 6(a) to the steady state (4.4) more closely. The temperature gradient is approximately constant in the steady state, so the solid curve ($t = 30$ ms) in Figure 6(a) should be roughly a straight line as it is, though not exact. In fact we can show that the curvature of the temperature field matches excellently with the nonlinearity revealed in (4.4). In order to visualize the nonlinearity of the temperature distribution, define

$$y = \ln\left(1 + \frac{c_p}{L}(T_s - T)\right).$$

From (4.4), for the steady state

$$y_{st} = \frac{Mc_p}{\kappa}(x - x_{ph}) \tag{4.5}$$

is a linear function of x. y_{st} and the y from the simulation at $t = 30$ ms are compared in Figure 7. The match is very accurate, which indicates that the state at $t = 30$ ms is close to the steady state in fine details. In conclusion, we have shown that our

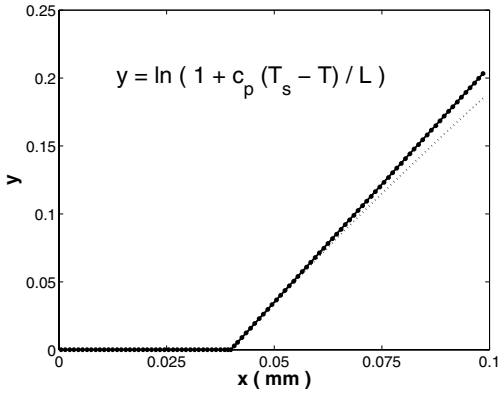

FIG. 7. *Match of the nonlinearity between the temperature from simulation at* $t = 30$ *ms and the steady state temperature distribution. The solid line is a plot of* y_{st} *in* (4.5). *The dots are the discretized values of* y *from simulation. The dotted line is the plot of* y *if the temperature gradient were constant. Obviously the actual* T *at* $t = 30$ *is much closer to* (4.4) *than a linear distribution.*

numerical algorithm for phase transitions in compressible fluids works equally well in advection-dominated and thermal wave-dominated regimes.

4.5. A problem coupling phase transitions and acoustic waves. In this test problem we show that, when acoustic wave and phase nonequilibrium are both present, as may occur in many practical situations, the dynamics of two-phase flows is strongly affected by both acoustic waves and phase transitions. As a contrast to sections 4.1–4.3, it will be shown that solutions in this section would be significantly changed if phase transitions were neglected.

The test problem is the condensation of oversaturated water vapor in the presence of an acoustic wave. Initially, both phases have length 2 cm. Vapor is on the left side, and water on the right side, with the phase boundary at the origin. The end of the domain on the water side is a reflection boundary, while the end on the vapor side is in contact with fixed ambient pressure. Both ends are insulated so there is no external heating or cooling. Both phases are at rest and have common temperature 293 K at the beginning. The initial vapor pressure is 93 mbar, whose saturation temperature is 343 K. The water pressure is 193 mbar. If the phase transition were neglected, the water first expands due to its higher pressure and then shrinks and expands periodically as the pressure wave propagates back and forth in the liquid. The temperature and velocity fluctuations would be small in both phases. When the phase transition is included in the process, the liquid volume still oscillates, but the oscillation is superposed upon an expansion due to condensation as the vapor is oversaturated. The temperature and velocity fluctuations are much stronger, especially in the vapor phase.

Figure 8 compares the evolution of the interface with and without phase transitions. Clearly the liquid volume oscillates while expanding when phase transition is included. It can be noticed that the expansion gradually slows down due to the lack of external cooling. Figure 9 plots the pressure, temperature, and velocity distributions at 1 microsecond. In all figures, solid lines are for phase transitions, while dashed lines are for a simple contact. In the pressure plot Figure 9(a) the dotted line shows the initial pressure distribution. In the temperature plot Figure 9(b) the horizontal line near the top stands for the initial saturation temperature of the vapor phase.

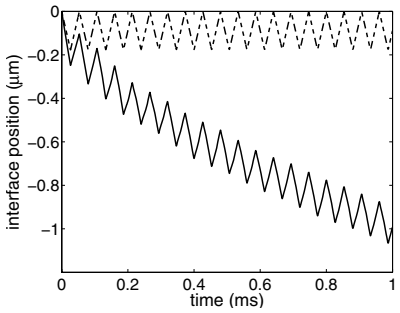

FIG. 8. *The evolution of the interface between water and water vapor in the presence of an acoustic wave. The solid line is for the process including a phase transition; the dashed line is for simple contact.*

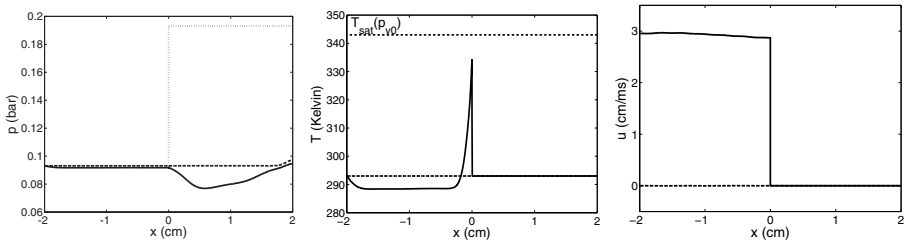

(a) (b) (c)

FIG. 9. *The pressure, temperature, and velocity distribution in water vapor and water at* 1 *microsecond. Solid lines are for the process including a phase transition; dashed lines are for simple contact. In* (a), *the dotted line shows the initial pressure distribution. In* (b), *the horizontal line near the top stands for the initial saturation temperature of the vapor phase.*

The temperature peak in the center is due to the heat released from condensation at the phase boundary. The interface temperature gradually approaches the saturation temperature. Eventually these temperatures coincide, and the motion of the phase transition stops as it does in all insulated systems. In Figure 9(c) the discontinuity in the center is from the mass flux across the phase boundary. It is clear from the figures that phase transitions play an important role when there is deviation from phase equilibrium.

4.6. Extension to higher dimensions. We have extended this method to higher dimensions based on the operator-splitting method for the front propagation. The subgrid model is applied along the interface normal direction. Here we present the 2D simulation of a vapor bubble expanding in tensile water. The computational domain is 0.32 cm $\times$ 0.24 cm. The domain is filled with water, and an elliptic vapor bubble initially rests at the center of the domain. The two half axes of the vapor bubble are 0.1 and 0.06 cm, respectively. The vapor bubble is saturated initially, having pressure 23.4 mbar at temperature 293.4 K. The ambient water is initially under 200 bar tension at temperature 293.2 K. The water evaporates, and the vapor bubble grows under the tension.

We compared the bubble growth in simulations of various resolutions. The bubble shape at time 1 μs is shown in Figure 10(a). The bubble area has increased by

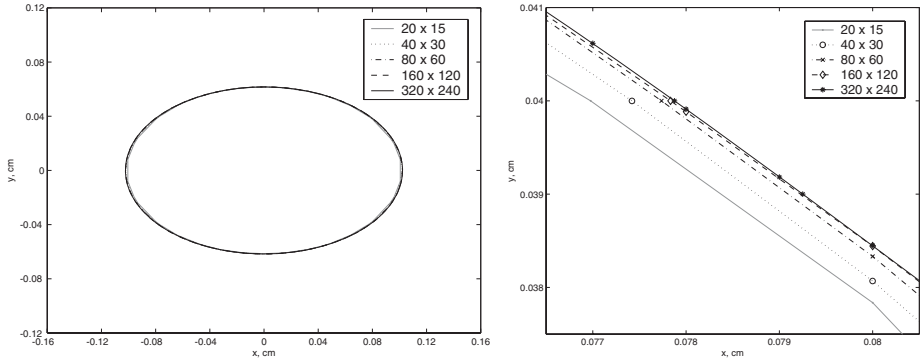

(a) (b)

FIG. 10. *Growth of a vapor bubble in tensile water.* (a) *shows the shape of the bubble at time* 1 μs. (b) *is the magnified view of (a) that shows the difference between the simulation results of various resolutions.*

TABLE 5
Accuracy and convergence rate of the bubble growth under tensile water.

	$t = 1$ μs			$t = 2$ μs		
$N_x \times N_y$	Area(cm^2)	Error	Order	Area(cm^2)	Error	Order
20×15	0.019476	3.40E-4	-	0.020678	6.81E-4	-
40×30	0.019688	1.28E-4	1.408	0.021073	2.87E-4	1.249
80×60	0.019769	4.68E-5	1.453	0.021243	1.17E-4	1.295
160×120	0.019802	1.41E-5	1.735	0.021321	3.86E-5	1.599

5.13% from the initial size. The bubble surfaces from various simulations are almost indistinguishable in Figure 10(a). In the magnified view in Figure 10(b) the difference in the fronts and the convergence under mesh refinement is clearer. Table 5 compares the bubble area at times 1 and 2 μs calculated from the simulations. The area calculated from the simulation of the highest resolution (320×240) is used as the reference value to determine the accuracy of other simulations. At time 2 μs the bubble has grown by 13.3% from the original size. The comparison confirms that the algorithm propagates the front with more than first order accuracy.

The method developed in this paper has been applied to resolve the dynamics at cavitation bubble surfaces in the simulations of the atomization of a high speed jet in the 2D axisymmetric geometry [33]. A plot of jet interface at late time is shown in Figure 11. This flow is strongly compressible, and vapor bubbles are created constantly. The capabilities developed here is necessary to carry out the simulations of the jet breakup.

5. Conclusions. We have proposed a new numerical method to the solution of phase boundaries for compressible flows. The method is based on the interface-tracking technique. We have presented one-dimensional simulations in different physical regimes as well as a two-dimensional simulation of bubble growth in tensile liquid to validate the method. The ability of the method to deal with complex interface is demonstrated through the simulation of atomization of a high speed jet. The algorithm is more than first order accurate everywhere including the tracked phase boundaries. From test problems presented in this paper, we see that the proposed

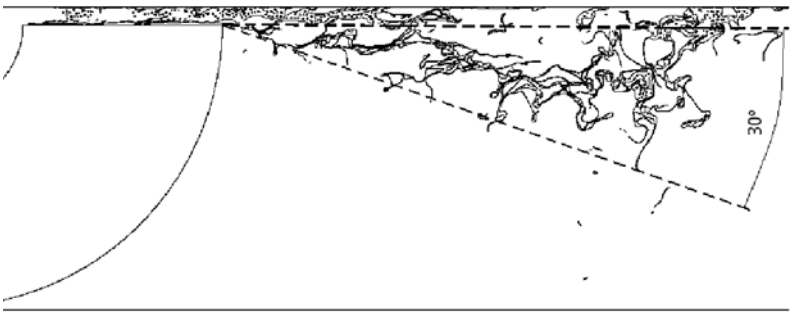

FIG. 11. *Plot of jet interface at late time.*

algorithm makes accurate predictions for problems ranging from advection-dominated ones, in which phase transitions play a minor role, to those with sustained thermal waves, in which phase transitions play a critical role, and to those coupled ones in which both phase transitions and hydro waves play important roles.

REFERENCES

[1] T. ALTY AND C. A. MACKAY, *The accommodation coefficient and the evaporation coefficient of water*, Proc. R. Soc. Lond. Ser. A, 149 (1935), pp. 104–116.

[2] B. BUKIET, C. L. GARDNER, J. GLIMM, J. W. GROVE, J. JONES, O. MCBRYAN, R. MENIKOFF, AND D. H. SHARP, *Applications of front tracking to combustion, surface instabilities and two-dimensional Riemann problems*, in Transactions of the Third Army Conference on Applied Mathematics and Computing, ARO report 86–1, 1986, pp. 223–243.

[3] G. CAGINALP, *An analysis of a phase field model of a free boundary*, Arch. Ration. Mech. Anal., 92 (1986), pp. 205–245.

[4] G. CAGINALP, *Higher-order phase field models and detailed anisotropy*, Phys. Rev. B, 34 (1986), pp. 490–4945.

[5] V. P. CAREY, *Liquid-Vapor Phase-Change Phenomena*, Hemisphere Publishing, New York, 1992.

[6] A. CHORIN AND J. MARSDEN, *A Mathematical Introduction to Fluid Mechanics*, 3rd ed., Springer-Verlag, Berlin, 1990.

[7] P. COLELLA, *A direct Eulerian MUSCL scheme for gas dynamics*, SIAM J. Sci. Comput., 6 (1985), pp. 104–117.

[8] J. GLIMM, M. J. GRAHAM, J. W. GROVE, X. L. LI, T. M. SMITH, D. TAN, F. TANGERMAN, AND Q. ZHANG, *Front tracking in two and three dimensions*, Comput. Math. Appl., 35 (1998), pp. 1–11.

[9] J. GLIMM, J. W. GROVE, X. L. LI, K.-M. SHYUE, Y. ZENG, AND Q. ZHANG, *Three-dimensional front tracking*, SIAM J. Sci. Comput., 19 (1998), pp. 703–727.

[10] J. GLIMM, J. W. GROVE, X. L. LI, AND D. C. TAN, *Robust computational algorithms for dynamic interface tracking in three dimensions*, SIAM J. Sci. Comput., 21 (2000), pp. 2240–2256.

[11] J. GLIMM, X. L. LI, AND Y. J. LIU, *Conservative front tracking and level set algorithms*, Proc. Natl. Acad. Sci. USA, 98 (2001), pp. 14198–14201.

[12] J. GLIMM, X. L. LI, AND Y. J. LIU, *Conservative front tracking in one space dimension*, Contemp. Math., 295 (2002), pp. 253–264.

[13] J. GLIMM, X. L. LI, Y. J. LIU, Z. L. XU, AND N. ZHAO, *Conservative front tracking with improved accuracy*, SIAM J. Numer. Anal., 41 (2003), pp. 1926–1947.

[14] D. E. HAGEN, J. SCHMITT, M. TRUEBLOOD, J. CARSTENS, D. R. WHITE, AND D. J. ALOFS, *Condensation coefficient measurement for water in the UMR cloud simulation chamber*, J. Atmopheric Sci., 46 (1989), p. 803.

[15] Y. HAO AND A. PROSPERETTI, *The dynamics of vapor bubbles in acoustic pressure fields*, Phys. Fluids, 11 (1999), pp. 2008–2019.

[16] A. HUANG AND D. D. JOSEPH, *Instability of the equilibrium of a liquid below its vapor between horizontal heated plates*, J. Fluid Mech., 242 (1992), pp. 235–247.

[17] D. Juric and G. Tryggvason, *Computations of boiling flows*, Int. J. Multiphase Flow, 24 (1998), pp. 387–410.
[18] B. van Leer, *Toward the ultimate conservative difference scheme:* III. *Upstream-centered finite-difference schemes for ideal compressible flow*, J. Comput. Phys., 23 (1977), pp. 263–275.
[19] S. Maruyama, T. Kurashige, S. Matsumoto, Y. Yamaguchi, and T. Kimura, *Liquid droplet in contact with a solid surface*, Thermophys. Eng., 2 (1998), pp. 49–62.
[20] Y. Matsumoto and F. Takemura, *Influence of internal phenomena on gas bubble motion*, JSME Int. J., B37 (1994), pp. 288–296.
[21] R. Menikoff and B. Plohr, *The Riemann problem for fluid flow of real materials*, Rev. Mod. Phys., 61 (1989), pp. 75–130.
[22] M. S. Plesset and S. A. Zwick, *The growth of vapor bubbles in superheated liquids*, J. Appl. Phys., 25 (1954), pp. 493–500.
[23] M. S. Plesset and A. Prosperetti, *Vapor bubble growth in a superheated liquid*, J. Appl. Phys., 85 (1978), pp. 349–368.
[24] A. Preston, *Modelling Heat and Mass Transfer in Bubbly Cavitating Flows and Shock Waves in Cavitating Nozzles*, Ph.D. thesis, California Institute of Technology, Pasadena, CA, 2004.
[25] A. Preston, T. Colonius, and C. E. Brennen, *Toward efficient computation of heat and mass transfer effects in the continuum model for bubbly cavitating flows*, in Proceedings of the Fourth International Symposium on Cavitation (CAV2001), session B4.002, Caltech, Pasadena, CA, 2001.
[26] Lord Rayleigh, *On the pressure developed in a liquid during the collapse of a spherical cavity*, Philos. Mag., 34 (1917), pp. 94–98.
[27] R. Richtmyer and K. Morton, *Difference Methods for Initial Value Problems*, 2nd ed., Interscience, New York, 1967.
[28] L. I. Rubinstein, *The Stefan Problem*, Trans. Math. Monographs 27, AMS, Providence, RI, 1971.
[29] S. Sinha, F. B. Jonathan, and V. K. Dhir, *Molecular dynamics simulation of interfacial tension of ultra-thin liquid films on a solid surface*, in Proceedings of the 2001 ASME International Mechanical Engineering Congress and Exposition (IMECE'01), ASME, New York, NY, 2001.
[30] G. Son and V. K. Dhir, *Numerical simulation of film boiling near critical pressures with a level set method*, J. Heat Transfer, 120 (1998), pp. 183–192.
[31] K. E. Starling, *Fluid Thermodynamic Properties for Light Petroleum Systems*, Gulf Publishing, Houston, TX, 1973.
[32] S. W. Welch, *Local simulation of two-phase flows including interface tracking with mass transfer*, J. Comput. Phys., 121 (1995), pp. 142–154.
[33] Z. L. Xu, M. Kim, T. Lu, W. Oh, J. Glimm, R. Samulyak, X. L. Li, and C. Tzanos, *Discrete bubble modeling of unsteady cavitating flow*, Int. J. Multiscale Comp. Eng., 4 (2006), pp. 601–616.